JBC RESEARCH ARTICLE

# New insights into P2X7 receptor regulation: $Ca^{2+}$-calmodulin and GDP bind to the soluble P2X7 ballast domain

Received for publication, March 17, 2022, and in revised form, September 9, 2022 Published, Papers in Press, September 15, 2022,
https://doi.org/10.1016/j.jbc.2022.102495

**Simon Sander[1], Isabel Müller[2], Maria M. Garcia-Alai[3], Annette Nicke[2], and Henning Tidow[1,*]**

*From the [1]Department of Chemistry, The Hamburg Advanced Research Centre for Bioorganic Chemistry (HARBOR), Institute for Biochemistry and Molecular Biology, University of Hamburg, Hamburg, Germany; [2]Faculty of Medicine, Walther Straub Institute of Pharmacology and Toxicology, LMU Munich, Munich, Germany; [3]European Molecular Biology Laboratory Hamburg, Hamburg, Germany*

Edited by Roger Colbran

**P2X7 receptors are nonselective cation channels that are activated by extracellular ATP and play important roles in inflammation. They differ from other P2X family members by a large intracellular C-terminus that mediates diverse signaling processes that are little understood. A recent cryo-EM study revealed that the C-terminus of the P2X7 receptor forms a unique cytoplasmic ballast domain that possesses a GDP-binding site as well as a dinuclear $Zn^{2+}$ site. However, the molecular basis for the regulatory function of the ballast domain as well as the interplay between the various ligands remain unclear. Here, we successfully expressed a soluble trimeric P2X7 ballast domain (P2X7BD) and characterized its ligand binding properties using a biophysical approach. We identified calmodulin (CaM)-binding regions within the ballast domain and found that binding of $Ca^{2+}$-CaM and GDP to P2X7BD have opposite effects on its stability. Small-angle X-ray scattering experiments indicate that $Ca^{2+}$-CaM binding disrupts the trimeric state of P2X7BD. Our results provide a possible framework for the intracellular regulation of the P2X7 receptor.**

Ligand-gated P2X receptor ion channels (1, 2) and G-protein–coupled P2Y receptors (3) are the two main classes of membrane proteins that mediate ATP-induced purinergic signaling (4). P2X receptors are trimeric, nonselective cation channels activated by extracellular ATP that are found in a variety of eukaryotic cells (5).

Within the mammalian P2X receptor family (P2X1 to P2X7), the homotrimeric P2X purinoreceptor 7 (P2X7R) contains unique functional properties: It requires high micromolar to millimolar ATP concentrations for activation (1 to 3 orders of magnitude higher than other P2X receptors) and shows a complete lack of desensitization (6–8). In addition, it contains a long intracellular C-terminus that is involved in a variety of signaling cascades. For example, the P2X7R can act as a cytotoxic receptor by inducing membrane permeabilization and eventually cell death (9–12).

Its involvement in inflammation, autoimmune diseases, neurodegenerative diseases, and cancer makes the P2X7R a promising pharmacological target (13–19).

A variety of proteins have been found to physically or functionally interact with the P2X7R and influence its diverse properties and signaling pathways (reviewed in (20)). One of the proteins that was found in functional and pull-down studies to interact with the rat P2X7R is the multifunctional messenger protein calmodulin (CaM). CaM acts as a $Ca^{2+}$ sensor translating $Ca^{2+}$ signals into cellular processes (21). A 1-5-16 CaM-binding motif ($IX_3LX_{10}W$) in the C-terminus of the rat P2X7R (aa I541-R557) was identified (22). Chelation of $Ca^{2+}$ or mutation of the CaM-binding site in the rat P2X7R influenced current facilitation of P2X7R (a P2X7R-specific property that describes the increase of agonist sensitivity and current amplitude upon repeated agonist application) and P2X7R-induced membrane blebbing, but did not interfere with dye uptake, an assay for P2X7R-induced membrane permeabilization. In the human ortholog, neither the binding motif nor a $Ca^{2+}$-dependent current facilitation could be detected, and it remains unclear whether CaM interacts with the human P2X7R (23). However, $Ca^{2+}$-dependent current facilitation could be reconstituted in the human P2X7R by replacing three critical residues (aa 541, 552, 559) with the respective residues of the identified rat CaM-binding domain.

Using cryo-EM, the structure of the full-length rat P2X7R has been recently determined in the apo as well as the ATP-bound state (8). This revealed for the first time the structure of the cytoplasmic part (8), which consists of a cytoplasmic cap, a Cys-anchor that prevents desensitization by anchoring to the membrane through palmitoylation, and a ballast domain located beneath the neighboring P2X7R subunit. This ballast domain is formed by the C-terminal 200 residues (α9-α16/β16-β18) and contains a GDP/GTP-binding site and a dinuclear $Zn^{2+}$ binding motif (8). Deletion of the C-terminal region has been shown to alter the function of the P2X7R, in particular with respect to pore dilation and initiation of cytolytic signal transduction (9, 12, 24).

In this study, we aimed to investigate the ligand-binding properties of the P2X7R ballast domain (P2X7BD) in more detail to better understand its modulatory role. We identified

* For correspondence: Henning Tidow, tidow@chemie.uni-hamburg.de.

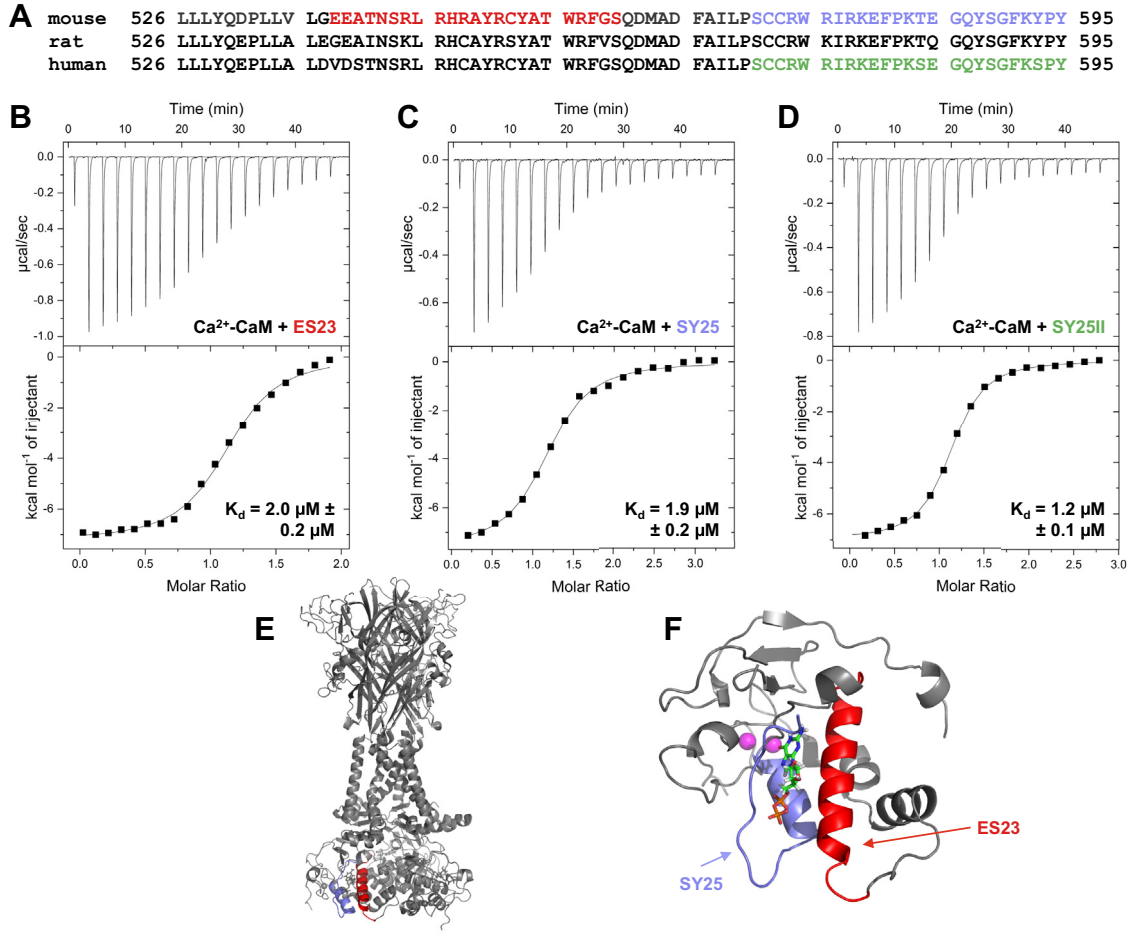


**Figure 1. P2X7R ballast domain contains two calmodulin-binding regions.** *A*, partial sequence alignment of C-terminal mouse, rat, and human P2X7R ballast domain (residues 526–595). Peptides used for binding studies are colored and named by first and last amino acid alongside length. *B–D*, ITC measurements of $Ca^{2+}$-CaM (20 µM) and the peptides (500 µM) from (*A*) revealed exothermic binding patterns with low µM $K_d$s. Details are listed in Table S1. Representative measurements are shown. *E* and *F*, mapping of calmodulin binding sites on the structures of the full length P2X7R (pdb: 6U9V) in (*E*) and the isolated ballast domain in (*F*). Peptides are color-coded as in (*A*), GDP and $Zn^{2+}$ ions are shown as *sticks* and *spheres*, respectively, in (*F*). ITC, isothermal titration calorimetry; P2X7R, homotrimeric P2X purinoreceptor 7.

potential CaM-binding regions within the rat, human, and mouse P2X7BDs and confirmed binding of two of the respective peptides to CaM. Using a soluble ballast domain, we determined the binding properties of both $Ca^{2+}$-CaM and GDP using various biophysical methods. We found that binding of $Ca^{2+}$-CaM and GDP to the human P2X7BD has opposite effects on the stability of the ballast domain. Further, small-angle X-ray scattering (SAXS) experiments indicate that $Ca^{2+}$-CaM-binding disrupts the trimeric state of the P2X7BD. These results provide a possible framework for the regulation of P2X7 receptor properties by its ballast domain.

## Results and discussion

### *The P2X7BD contains two CaM-binding regions*

As CaM was shown to bind to the C-terminus of the rat but not human P2X7R (22), we initially set out to confirm and identify the exact binding site in the human, mouse, and rat P2X7R sequences, respectively, using P2X7R-derived peptides. Based on an appropriate spacing of hydrophobic anchor residues required for efficient $Ca^{2+}$-CaM binding (25), we identified two P2X7R sequences as putative CaM-binding regions (aa 538–560 and 571–595, Fig. 1*A*). Isothermal titration calorimetry (ITC) experiments using the corresponding peptides from the C-terminus of the mouse and human P2X7R revealed binding of $Ca^{2+}$-CaM to three peptides with low-micromolar $K_d$ (Fig. 1, *B–D* and Table S1). The remaining peptides from human and rat were insoluble. When mapped on the structure of the recently determined cryo-EM structure of the full-length rat P2X7R, it became obvious that the peptides correspond to two helical regions within the P2X7BD that are both involved in GDP coordination (Fig. 1, *E* and *F*).

In order to investigate whether $Ca^{2+}$-CaM also binds to these sites in the context of the entire ballast domain, we recombinantly expressed and purified the human P2X7BD (residues 395–595, $M_W$ = 24.6 kDa). This construct starts directly after the cytoplasmic cap region as identified by McCarthy *et al.* (8) and extends to the C-terminus of the full-length P2X7R. The corresponding protein could be expressed in *E. coli* and purified to homogeneity, showing a monodisperse size-exclusion chromatography (SEC) profile (Fig. 2*A*, black trace). The elution volume indicates a trimeric assembly

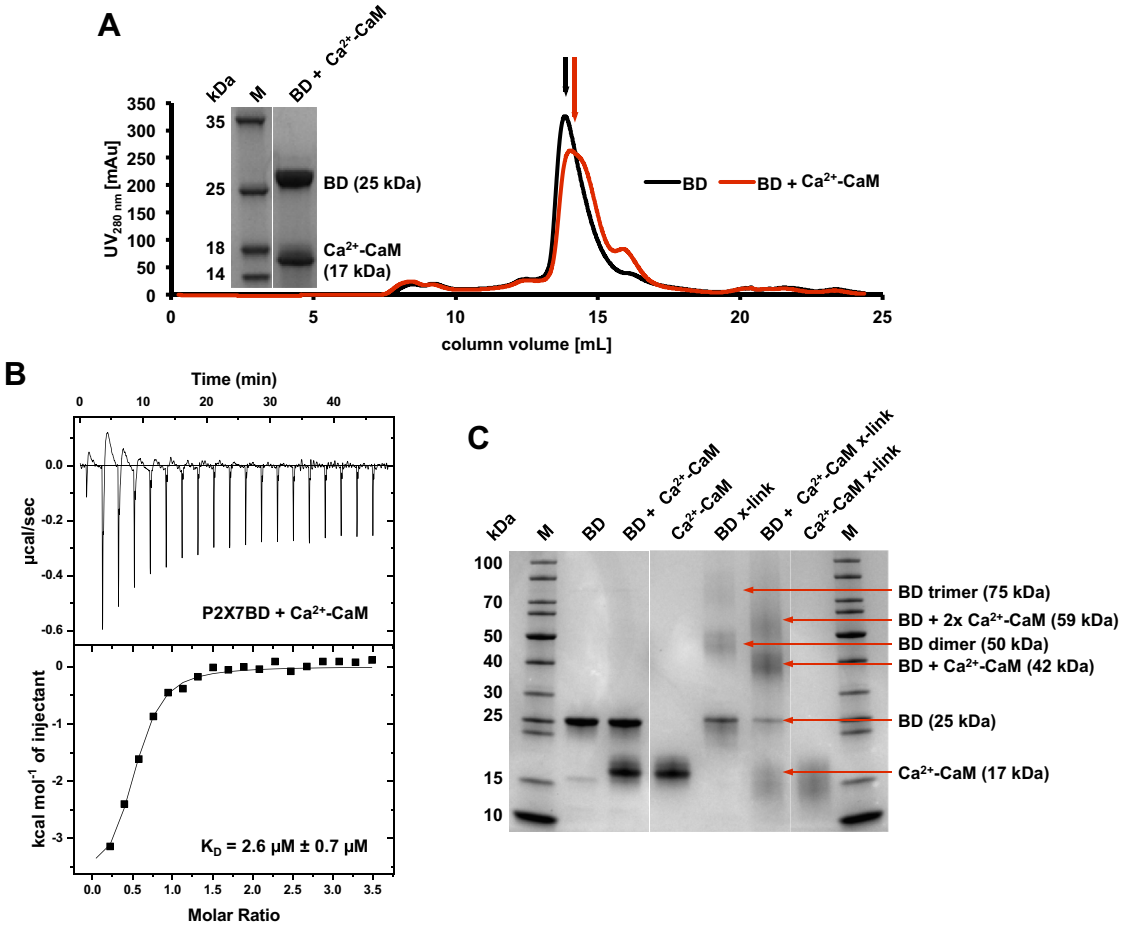


**Figure 2. $Ca^{2+}$-calmodulin ($Ca^{2+}$-CaM) binds to the intact P2X7R ballast domain (P2X7BD).** *A*, size-exclusion chromatography indicates trimeric state for human P2X7BD (short: BD, *black trace*). Addition of $Ca^{2+}$-CaM to hP2X7BD (*red trace*) resulted in complex formation (see SDS-PAGE inset) that eluted at slightly higher volume indicating smaller molecular weight and thus a disruption of the trimeric state upon $Ca^{2+}$-CaM binding. Representative curves of triplicate experiments are shown. *B*, ITC measurement of intact BD (35 µM) and $Ca^{2+}$-CaM (670 µM) reveals exothermic binding in the low micromolar range ($K_d$ ± fitting error). Details are listed in Table S1. Representative measurement of a duplicate is shown. *C*, chemical crosslinking assay using disuccinimidyl suberate followed by SDS-PAGE. Identity of the different bands was confirmed by tryptic digest and mass spectrometry (see Table 2). Inputs as well as complex bands are labeled. Results indicate $Ca^{2+}$-CaM-binding disrupts the P2X7BD trimeric state and leads to a state where one or two $Ca^{2+}$-CaM molecules bind to monomeric ballast domain. ITC, isothermal titration calorimetry; P2X7R, homotrimeric P2X purinoreceptor 7.

state for the human P2X7BD (short: BD), in good agreement with the known trimeric P2X receptor structure and the cryo-EM structure of the rat P2X7R, which revealed substantial interactions between the ballast domains (despite the absence of 27 residues (aa 443–469) that could not be modeled due to lack of density and are probably unfolded as indicated by the AlphaFold2 model) (8). Addition of recombinant $Ca^{2+}$-CaM to the P2X7BD caused a slight shift toward higher elution volume during SEC analysis, indicating that the P2X7BD/$Ca^{2+}$-CaM complex is smaller than the ballast domain alone and that its trimeric state is altered or disrupted upon $Ca^{2+}$-CaM binding (Fig. 2*A*, red trace). ITC data confirmed the interaction between $Ca^{2+}$-CaM and the P2X7BD and revealed binding in the low micromolar range (Fig. 2*B* and Table S1). Although this binding is exothermic, the change in total enthalpy (–3.9 kcal/mol) is significantly smaller compared to $Ca^{2+}$-CaM binding to the individual peptides (–7.0 kcal/mol, see Fig. 1, *B–D* and Table S1). The reaction seems to be mainly driven by the change in entropy, providing further indication for a $Ca^{2+}$-CaM–mediated P2X7BD trimer alteration/disruption.

Chemical cross-linking of the P2X7BD with disuccinimidyl suberate followed by SDS-PAGE identified three bands at 25 kDa, 50 kDa, and 75 kDa that we assigned to monomeric, dimeric, and trimeric ballast domain (Fig. 2*C*, theoretical values: Table 1). In the presence of $Ca^{2+}$-CaM (17 kD), a distinct pattern of the cross-linked proteins was observed. In addition to monomeric P2X7BD at 25 kDa, two new bands at around 40 kDa and between 50 kDa and 60 kDa could be detected (Fig. 2*B*, lane "BD + $Ca^{2+}$-CaM x-link") in good agreement with P2X7BD/$Ca^{2+}$-CaM complexes in the ratios

**Table 1**
**Theoretical molecular weights (MWs) of P2X7BD and $Ca^{2+}$-CaM and possible complexes**

| Protein (complex) | Theoretical MW [kDa] |
|---|---|
| $Ca^{2+}$-CaM | 16.7 |
| P2X7BD trimer | 73.8 |
| P2X7BD + $Ca^{2+}$-CaM (1:1) | 41.3 |
| P2X7BD + $Ca^{2+}$-CaM (1:2) | 58.0 |

Calculations are based on the amino acid sequences of the expressed proteins.

1:1 (41 kD) and 1:2 (58 kD). In support of this, mass spectrometric analysis of tryptic digests of these bands confirmed the presence of both P2X7BD and CaM peptides (Table 2) in these bands. The absence of larger complexes could indicate that $Ca^{2+}$-CaM binding disrupts the P2X7BD trimeric state and leads to a state where one or two $Ca^{2+}$-CaM molecules bind to the monomeric ballast domain.

### *Binding of $Ca^{2+}$-CaM and GDP to the P2X7BD has opposite effects on the stability of the ballast domain*

Next, we used nano differential scanning fluorimetry (nDSF) to investigate the effect of $Ca^{2+}$-CaM or GDP binding on the stability of the human P2X7BD. nDSF follows intrinsic tryptophan fluorescence as a function of temperature and reports on protein (un)folding and conformational changes as a consequence of changes in the tryptophan environment (26, 27). As CaM does not contain any tryptophan or tyrosine residues, it does not contribute to the nDSF signal during complex analysis (Fig. S1).

The soluble P2X7BD exhibits an apparent melting temperature ($T_m$) of 43.3 °C ± 0.1 °C (n = 3, Fig. 3, *A* and *B*, blue trace). Concentration-dependent $T_m$ experiments indicate a small concentration-dependent stabilization of P2X7BD (Fig. S2). In the presence of increasing $Ca^{2+}$-CaM concentrations, a huge drop in $T_m$ can be observed (up to >10 °C) (Fig. 3, *A* and *B*, green trace). This destabilization of P2X7BD caused by $Ca^{2+}$-CaM binding could be explained by disruption of the P2X7BD trimeric state, in support of our observations in the cross-linking experiment (see Fig. 2*C*). In the monomeric $Ca^{2+}$-CaM complex, the P2X7BD is less stable than in its native trimeric state. The scattering data indicate that apo-P2X7BD and P2X7BD/GDP start to aggregate once the proteins unfold (Fig. 3*C*, blue and red traces). However, in the presence of $Ca^{2+}$-CaM, the P2X7BD samples do not aggregate anymore (Fig. 3*C*, green trace), indicating that $Ca^{2+}$-CaM binding to P2X7BD prevents it from aggregation. Interestingly, apo-CaM (with EDTA instead of $Ca^{2+}$) does not change the melting temperature of P2X7BD (Fig. 3*D*), indicating that apo-CaM does not bind to the protein target as observed for many other CaM-regulated proteins (25).

As the cryo-EM structure of rat P2X7 identified an unexpected binding site for GDP within the ballast domain (8), we also investigated the effect of GDP on human P2X7BD stability. GDP binds to P2X7BD with a $K_d$ of 2.6 μM ± 0.2 μM as measured by ITC (n = 3, Fig. 3*E*). nDSF analysis revealed a strong stabilizing effect of GDP with the $T_m$ of P2X7BD increasing from 43.3 °C ± 0.1 °C in absence to 51.0 °C ± 0.1 °C in the presence of 1 mM GDP (n = 3, Fig. 3, *A–C*, red trace).

A joint analysis of $Ca^{2+}$-CaM binding and GDP binding to P2X7BD by nDSF resulted in similar (de)stabilization curves, however with shifts in absolute $T_m$ values (Fig. 3, *F* and *G*). Isothermal analysis and affinity quantification based on these nDSF thermal shifts (28, 29) yielded similar $K_d$s for GDP independent of the $Ca^{2+}$-CaM concentration. These results can be explained by reversible binding events, where $Ca^{2+}$-CaM and/or GDP bind to P2X7BD and the equilibrium can be shifted based on relative concentrations and dissociation constants ($K_d$) (Fig. 4*A*). In summary, these data suggest that $Ca^{2+}$-CaM but not apo-CaM promotes dissociation of the BD, which is counteracted by a stabilizing effect of GDP.

The structure of the homologous rat ballast domain provides a plausible structural model for the ligand binding equilibrium: The C-terminal helix-loop structure (comprising peptide SY25, see Fig. 1*A*) is involved in GDP binding by clamping it in its binding pocket (Fig. 4*B*). Binding of $Ca^{2+}$-CaM to this region may disrupt this helix-loop structure and impair GDP binding.

### *$Ca^{2+}$-CaM binding disrupts the trimeric state of P2X7BD*

As our results presented above (nDSF, SEC, crosslinking, and ITC) already indicated that $Ca^{2+}$-CaM binding changes the oligomeric state of P2X7BD, we next used SEC-SAXS to further investigate the effect of $Ca^{2+}$-CaM binding on the overall structural parameters of the ballast domain (Fig. S3). The SAXS data of human P2X7BD yielded a radius of gyration ($R_g$) of 3.09 nm, a maximal protein dimension ($D_{max}$) of 10.49 nm, and a molecular weight estimate of 72.4 kDa, all in agreement with a trimeric state (Fig. 5*A* and Table 3). *Ab initio* modeling using DAMFILT also supports a trimeric state of human P2X7BD in solution (Fig. 5*B*).

For the P2X7BD/$Ca^{2+}$-CaM complex, the overall structural parameters obtained by SEC-SAXS changed significantly (Fig. 5*A* and Table 3). While $R_g$ and $D_{max}$ increased for the complex, the Porod volume and molecular weight decreased. These findings are in line with the data obtained by the other methods and indicate that $Ca^{2+}$-CaM binding to P2X7BD breaks its trimeric form resulting in a complex comprising one P2X7BD monomer with one or two $Ca^{2+}$-CaM molecules.

## Conclusion

Here we show for the first time the successful expression of a soluble trimeric P2X7BD, a domain that is unique within the P2X family (12) and also has no homology to any other

**Table 2**
**Mass spectrometric analysis of tryptic digest of bands after crosslinking**

| | P2X7BD | | CaM | |
|---|---|---|---|---|
| Band from crosslink | # Unique peptides | Detected peptide coverage | # Unique peptides | Detected peptide coverage |
| 40 kDa | 17 | 74% | 12 | 66% |
| 55 kDa | 16 | 74% | 10 | 65% |

SDS-PAGE gel bands were cut out and subjected to tryptic digest. Resulting peptides were subsequently analyzed by mass spectrometry and mapped to the sequences of the P2X7 ballast domain (P2X7BD) and calmodulin (CaM).

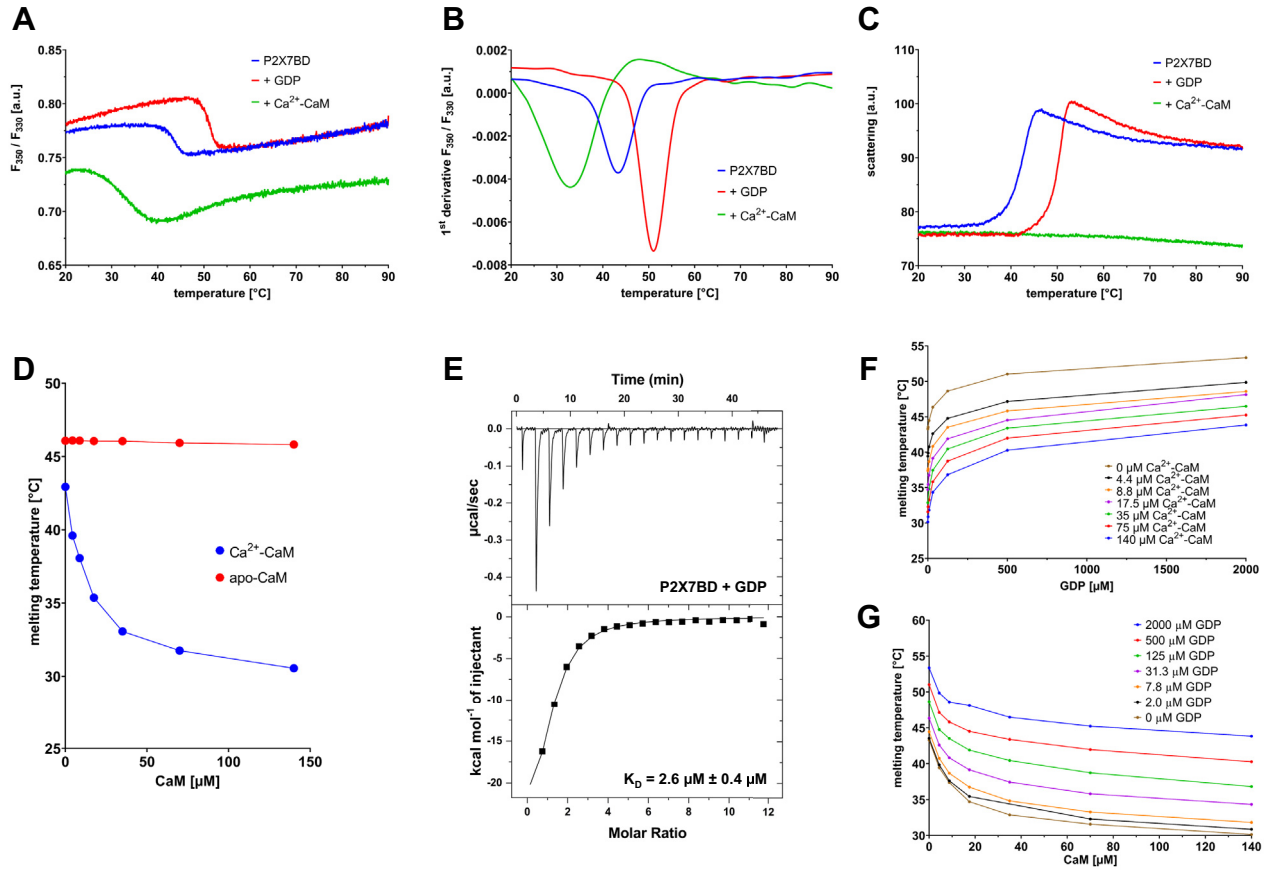


**Figure 3. Binding of $Ca^{2+}$-calmodulin ($Ca^{2+}$-CaM) and GDP to P2X7R ballast domain have opposite effects on the stability of the ballast domain.** *A–C*, nDSF analysis of P2X7BD (20 µM, *blue*) as well as of its complex with GDP (500 µM, *red*), $Ca^{2+}$-CaM (35 µM, *green*). Raw data $F_{350}/F_{330}$ (*A*), first derivatives $F_{350}/F_{330}$ (visualizing $T_m$ values as minima) (*B*) as well as scattering data (visualizing aggregation status) (*C*) indicate stabilization of P2X7BD by GDP and destabilization by $Ca^{2+}$-CaM. *D*, analysis of melting temperature by nDSF shows concentration-dependent destabilization of P2X7BD by $Ca^{2+}$-CaM (*blue trace*) but no effect by apo-CaM (*red trace*, with EDTA instead of $Ca^{2+}$). *E*, ITC measurement of P2X7BD (35 µM) with GDP (300 µM) reveals exothermic binding with a $K_d$ of 2.6 µM ± 0.2 µM. Representative measurement of a triplicate is shown. *F* and *G*, melting temperature analysis of P2X7BD by nDSF shows concentration-dependent destabilization by $Ca^{2+}$-CaM as well as stabilization by GDP. All nDSF data were performed in triplicates and representative, data are shown. ITC, isothermal titration calorimetry; nDSF, nano differential scanning fluorimetry; P2X7BD, P2X7R ballast domain; P2X7R, homotrimeric P2X purinoreceptor 7.

protein. We could further show that the human P2X7BD interacts reversibly with GDP and $Ca^{2+}$-CaM and that $Ca^{2+}$-CaM-binding disrupts the trimeric state of P2X7BD. However, the resulting implications for signaling and receptor gating in context of the full-length P2X7R remain elusive. Studies with a truncated P2X7R variant completely lacking the C-terminal ballast revealed that the domain is not directly involved in receptor gating since the mutant was behaving very similar to the wildtype P2X7R when analyzed by two-electrode voltage-clamp (8). However, some functional properties like the ability to induce membrane permeabilization as well as the activation of caspases (12, 13, 24) require the ballast domain. Therefore,

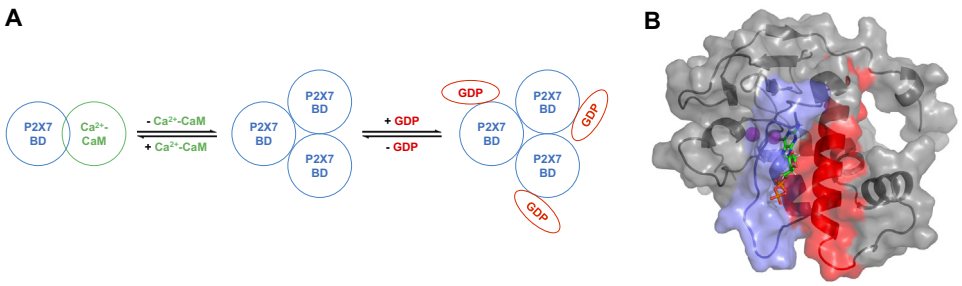


**Figure 4. Model for ligand binding to the P2X7R ballast domain.** *A*, schematic view of the equilibria of GDP and $Ca^{2+}$-calmodulin ($Ca^{2+}$-CaM) binding to the P2X7R ballast domain (P2X7BD). The trimeric form of P2X7BD is disrupted when $Ca^{2+}$-CaM is bound. *B*, the C-terminal helix-loop structure (*blue*) is involved in GDP binding by clamping it in its binding pocket. Binding of $Ca^{2+}$-CaM to this region may disrupt this helix-loop structure and impair binding of GDP. P2X7R, homotrimeric P2X purinoreceptor 7.

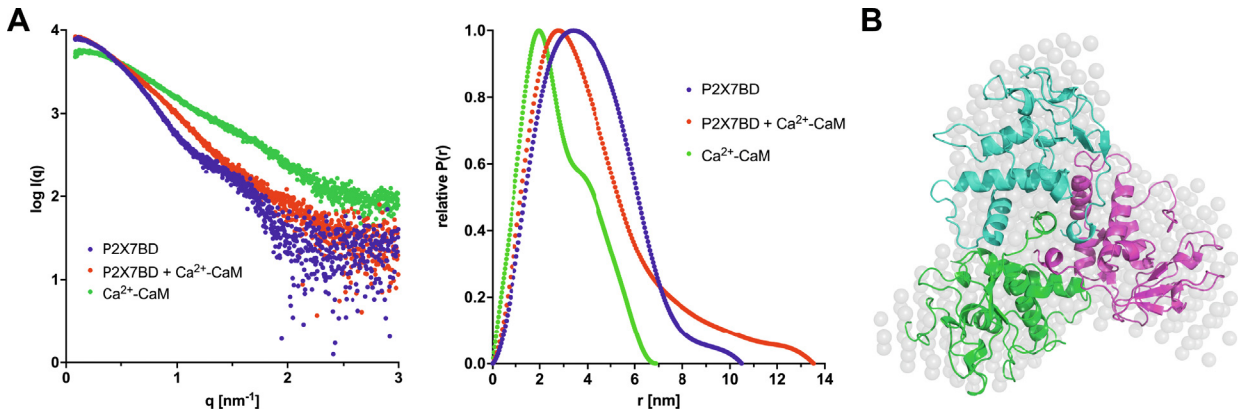


**Figure 5. SAXS analysis indicated that calmodulin-binding disrupts the trimeric state of P2X7BD.** *A*, SEC-SAXS raw data of buffer subtracted samples (*left*) and distance distribution plot (*right*) reveal conformational changes upon $Ca^{2+}$-CaM binding to P2X7BD. *B*, structure of trimeric P2X7BD (extracted from pdb: 6U9V) superimposed on *ab initio* DAMFILT model. P2X7BD, P2X7R ballast domain; P2X7R, homotrimeric P2X purinoreceptor 7; SAXS, small-angle X-ray scattering; SEC, size-exclusion chromatography.

it is very likely that the ballast domain connects the channel function of P2X7R to intracellular signaling cascades.

CaM seems to be one of these signaling proteins since it interacts with P2X7BD ((22) and this study). We observed a disruption of the P2X7BD trimer upon $Ca^{2+}$-CaM binding. If binding of $Ca^{2+}$-CaM to the full-length P2X7R also disrupts the trimeric state of the ballast domain within the full-length P2X7 receptor, this may induce conformational changes that are transmitted to the cytoplasmic cap and lead to altered functional properties of the receptor. The role of GDP in this process as well as its origin remains unclear. We showed that it binds to and stabilizes the isolated ballast domain and thus counteracts the destabilizing effect caused by $Ca^{2+}$-CaM–mediated dissociation of the trimeric state.

Taken together, this study provides first insights into the regulation of the P2X7 receptor by $Ca^{2+}$-CaM and GDP. The results form a basis for further studies on P2X7BD and the possible implications for ligand-controlled P2X7R signal transduction.

**Table 3**
**SEC-SAXS analysis of P2X7 ballast domain (P2X7BD) and $Ca^{2+}$-calmodulin ($Ca^{2+}$-CaM), alone and in complex**

| Sample details | P2X7BD | $Ca^{2+}$-CaM | P2X7BD/$Ca^{2+}$-CaM complex |
|---|---|---|---|
| SASBDB access code | SASDPE4 | SASDPD4 | SASDPF4 |
| Sample composition | 330 μM P2X7BD | 720 μM $Ca^{2+}$-CaM | 330 μM P2X7BD + 720 μM $Ca^{2+}$-CaM |
| Buffer composition | 20 mM Hepes pH 7.5, 150 mM NaCl, 5 mM $CaCl_2$ | | |
| SEC-SAXS parameters | 35 μl injected to an S200 increase 5/150 column, Agilent 1260Bio system, flow rate: 0.35 ml/min | | |
| Data acquisition parameters | | | |
| Instrument | EMBL P12 (PETRA III, DESY, Hamburg, Germany) | | |
| Detector | Dectris Pilatus 6M (2D photon counting detector) | | |
| Detector distance [m] | 3.0 | | |
| Beam geometry [$mm^2$] | 0.1 × 0.05 | | |
| Wavelength [nm] | 0.124 | | |
| q range [$nm^{-1}$] | 1–7 | | |
| Exposure time | 0.245 s per frame within 0.250 s exposure period, 2880 frames total | | |
| Temperature | 291 K | | |
| Structural parameters | | | |
| I(0) from P(r) [$cm^{-1}$] | 8204 ± 11 | 5926 ± 10 | 8613 ± 14 |
| $R_g$ from P(r) [nm] | 3.10 ± 0.01 | 2.20 ± 0.01 | 3.48 ± 0.01 |
| I(0) from Guinier [$cm^{-1}$] | 8216 ± 12 | 5879 ± 11 | 8501 ± 13 |
| $R_g$ from Guinier [nm] | 3.09 ± 0.01 | 2.13 ± 0.01 | 3.24 ± 0.01 |
| $D_{max}$ [nm] | 10.49 | 6.88 | 13.53 |
| Porod volume estimate [$Å^3$] | 94,246 | 22,713 | 72,532 |
| Molecular mass determination | | | |
| $MM_{QP}$ (from Porod invariant) [kDa] | 74.9 | 13.3 | 51.6 |
| MoW (from Porod invariant) [kDa] | 77.8 | 13.9 | 56.3 |
| From volume of correlation ($V_C$) [kDa] | 68.6 | 16.7 | 45.8 |
| From size & shape [kDa] | 72.7 | 17.0 | 53.5 |
| From Bayesian inference [kDa] | 72.4 | 15.5 | 50.8 |
| Software employed | | | |
| SEC-SAXS data processing | CHROMIXS (part of ATSAS 3.0) | | |
| Data processing | PRIMUS, including GNOM (part of ATSAS 3.0) | | |
| *Ab initio* analysis | DAMFILT (part of ATSAS 3.0) | | |
| 3D molecular graphics | PyMOL | | |

Details of the SEC-SAXS measurements, including sample details, data acquisition parameters, structural parameters, different methods for obtaining molecular mass estimates, and software employed. Data are presented according to the accepted guidelines for publication of SAXS data (35). All datasets were deposited in the SASBDB.

## Experimental procedures

### Materials

All chemicals were of analytical quality and purchased from Carl Roth or Sigma Aldrich, unless otherwise stated.

### Expression and purification of P2X7BD

A pET28a vector was used to express the cytoplasmic ballast domain (P2X7BD, residues 395–595) of the human P2X7R protein with a tobacco etch virus–cleavable C-terminal mCherry-$His_6$-tag. Protein expression was carried out in Rosetta 2 (DE3) cells in Terrific Broth medium. Cells were induced (0.1 mM IPTG) at a density of 0.6 (measured at 600 nm) and further grown at 20 °C for 16 h. After lysis using a high-pressure homogenizer (EmulsiFlex-C3, Avestin), the cleared lysate was subjected to immobilized metal affinity chromatography with Ni-NTA resin to purify the $His_6$-tagged fusion protein. Further purification was achieved by the removal of the mCherry-$His_6$-tag by tobacco etch virus protease, subsequent reverse Ni-NTA chromatography, and gel filtration on a Superdex S200 increase 10/300 column (Cytiva) using Hepes buffer (20 mM Hepes pH 7.5, 150 mM NaCl, 5 mM $CaCl_2$). Peak fractions of trimeric P2X7BD were pooled, and protein identity was confirmed by SDS-PAGE and mass spectrometry.

### Expression and purification of CaM

The sequence coding for human CaM was cloned into a pET15b vector without additional tags. Protein expression was carried out in BL21 Gold (DE3) cells in LB medium. Cells were induced (0.1 mM IPTG) at a density of 0.6 (measured at 600 nm) and further grown at 20 °C for 16 h. After lysis by pulsed sonication, the cleared lysate was subjected to hydrophobic interaction chromatography on a HiTrap Phenyl FF (LS) column (Cytiva). The following buffers were used: lysis and loading: 50 mM Tris pH 7.5, 2 mM $CaCl_2$; elution: 50 mM Tris pH 7.5, 10 mM EDTA. The eluted protein fractions were pooled and gel filtrated in Hepes buffer (see above) to obtain the active $Ca^{2+}$-CaM or in Hepes-EDTA buffer (20 mM Hepes pH 7.5, 150 mM NaCl, 10 mM EDTA) to obtain apo-CaM. Peak fractions were pooled, and protein identity was confirmed by SDS-PAGE and mass spectrometry.

### Isothermal titration calorimetry

ITC assays were carried out on a MicroCal ITC-200 isothermal titration calorimeter (Malvern Panalytical), and thermodynamic parameters were analyzed using the MicroCal ORIGIN software. The ligands (peptides, GDP, or $Ca^{2+}$-CaM) were diluted in Hepes buffer (see purification) to a concentration of 500 μM (peptides), 300 μM (GDP), or 670 μM ($Ca^{2+}$-CaM) and placed in the ITC syringe. After an initial injection of 0.5 μl, 18 regular injections of 2 μl were added to 20 μM $Ca^{2+}$-CaM or 35 μM P2X7BD in the sample cell. Each injection was interspaced by 150 s, and the stirring speed was set to 750 rpm. Heat of dilution was obtained by titrating ligand into buffer to allow for baseline correction. Binding curves were fitted using a one-site binding model.

### Protein cross-linking experiments

Purified P2X7BD (50 μM) was mixed with an equal amount of purified $Ca^{2+}$-CaM (50 μM) before the chemical cross-linker disuccinimidyl suberate was added at 50× excess (2.5 mM). After 30 min incubation at room temperature, 50 mM Tris pH 7.5 was added to quench the reaction, and the samples were analyzed by SDS-PAGE.

### Analytical SEC

Purified P2X7BD (250 μM) was mixed with 5× excess of purified $Ca^{2+}$-CaM (1250 μM) and incubated on ice for 30 min. The mixture was gel filtrated on a Superdex S200 increase 10/300 column (Cytiva) using Hepes buffer (20 mM Hepes pH 7.5, 150 mM NaCl, 5 mM $CaCl_2$). Fractions of the peaks were analyzed by SDS-PAGE and mass spectrometry.

### Nano differential scanning fluorimetry

Thermal protein unfolding was measured using a nanoDSF differential scanning fluorimeter (Prometheus, NanoTemper Technologies) allowing to monitor intrinsic tryptophan fluorescence. P2X7BD at a concentration of 20 μM was mixed with varying concentrations of GDP as well as $Ca^{2+}$-CaM. A thermal gradient from 20 to 95 °C with a heating rate of 1 °C/min was applied. All measurements were performed in triplicates (two biological replicates with three technical replicates each), and the ratio from fluorescence intensities measured at 350 nm and 330 nm was calculated in order to determine the melting temperatures of the complexes.

### Size-exclusion chromatography small-angle X-ray scattering

SEC-SAXS measurements were performed on the Bio-SAXS beamline P12 on the storage ring PETRA III (DESY). Samples were chromatographically separated using an S200 increase 5/150 column in Hepes buffer (see purification) before the measurement. SEC-SAXS data analysis was performed with CHROMIXS (30) as part of the ATSAS 3.0 package (31). Peaks were assigned based on the SEC information from the purification process. $R_g$, Porod volumes, and MW estimates were obtained from buffer subtracted scattering curves using the Guinier approximation (31). The distance distribution function (P(r)) and the $D_{max}$ were calculated from the entire scattering curve using the program GNOM (32). CRYSOL (33) was used to compare the experimental with theoretical scattering curves. Furthermore, *ab initio* models were generated using DAMMIF (34).

## Data availability

SAXS datasets were deposited in the SASBDB (access codes SASDPD4/SASDPE4/SASDPF4). All other data are available from the lead author upon reasonable request.

*Supporting information*—This article contains supporting information.

*Acknowledgments*—We thank members of the Nicke and Tidow labs for helpful discussions. We would like to acknowledge the assistance of the Core Facility Mass Spectrometric Proteomics of the UKE Hamburg supported in part by the DFG and the BMBF. The synchrotron SAXS data were collected at beamline P12 operated by EMBL Hamburg at the PETRA III storage ring (DESY, Hamburg, Germany). We acknowledge access to the Sample Preparation and Characterization (SPC) Facility of EMBL (Hamburg).

*Author contributions*—S. S., I. M., and M. M. G. A. investigation; S. S., A. N., and H. T. writing-original draft; A. N. and H. T. funding acquisition; A. N. and H. T. supervision; S. S. visualization; M. M. G. A. methodology; A. N. and H. T. conceptualization.

*Funding and additional information*—This research was funded by the Collaborative Research Centre SFB1328 (project A05 to H. T., project A15 to A. N.).

*Conflict of interest*—The authors declare that they have no conflicts of interest with the contents of this article.

*Abbreviations*—The abbreviations used are: ATP, adenosine triphosphate; CaM, calmodulin; $D_{max}$, maximal protein dimension; GDP, guanosine diphosphate; ITC, isothermal titration calorimetry; $M_W$, molecular weight; nDSF, nano differential scanning fluorimetry; P2X7R, P2X purinoreceptor 7; P2X7BD, P2X purinoreceptor 7 ballast domain; $R_g$, radius of gyration; SAXS, small-angle X-ray scattering; SEC, size-exclusion chromatography.

## References

1. Brake, A. J., Wagenbach, M. J., and Julius, D. (1994) New structural motif for ligand-gated ion channels defined by an ionotropic ATP receptor. *Nature* **371**, 519–523
2. Valera, S., Hussy, N., Evans, R. J., Adami, N., North, R. A., Surprenant, A., *et al.* (1994) A new class of ligand-gated ion channel defined by P2x receptor for extracellular ATP. *Nature* **371**, 516–519
3. Webb, T. E., Simon, J., Krishek, B. J., Bateson, A. N., Smart, T. G., King, B. F., *et al.* (1993) Cloning and functional expression of a brain G-protein-coupled ATP receptor. *FEBS Lett.* **324**, 219–225
4. Burnstock, G. (1976) Do some nerve cells release more than one transmitter? *Neuroscience* **1**, 239–248
5. Fountain, S. J., and Burnstock, G. (2009) An evolutionary history of P2X receptors. *Purinergic Signal.* **5**, 269–272
6. Jarvis, M. F., and Khakh, B. S. (2009) ATP-gated P2X cation-channels. *Neuropharmacology* **56**, 208–215
7. Koshimizu, T., Tomic, M., Koshimizu, M., and Stojilkovic, S. S. (1998) Identification of amino acid residues contributing to desensitization of the P2X2 receptor channel. *J. Biol. Chem.* **273**, 12853–12857
8. McCarthy, A. E., Yoshioka, C., and Mansoor, S. E. (2019) Full-length P2X7 structures reveal how palmitoylation prevents channel desensitization. *Cell* **179**, 659–670.e13
9. Costa-Junior, H. M., Sarmento Vieira, F., and Coutinho-Silva, R. (2011) C terminus of the P2X7 receptor: treasure hunting. *Purinergic Signal.* **7**, 7–19
10. Jiang, L. H., Caseley, E. A., Muench, S. P., and Roger, S. (2021) Structural basis for the functional properties of the P2X7 receptor for extracellular ATP. *Purinergic Signal.* **17**, 331–344
11. Rassendren, F., Buell, G. N., Virginio, C., Collo, G., North, R. A., and Surprenant, A. (1997) The permeabilizing ATP receptor, P2X7. Cloning and expression of a human cDNA. *J. Biol. Chem.* **272**, 5482–5486
12. Surprenant, A., Rassendren, F., Kawashima, E., North, R. A., and Buell, G. (1996) The cytolytic P2Z receptor for extracellular ATP identified as a P2X receptor (P2X7). *Science* **272**, 735–738
13. Adinolfi, E., Giuliani, A. L., De Marchi, E., Pegoraro, A., Orioli, E., and Di Virgilio, F. (2018) The P2X7 receptor: a main player in inflammation. *Biochem. Pharmacol.* **151**, 234–244
14. Bartlett, R., Stokes, L., and Sluyter, R. (2014) The P2X7 receptor channel: recent developments and the use of P2X7 antagonists in models of disease. *Pharmacol. Rev.* **66**, 638–675
15. Bhattacharya, A., and Biber, K. (2016) The microglial ATP-gated ion channel P2X7 as a CNS drug target. *Glia* **64**, 1772–1787
16. Burnstock, G., and Knight, G. E. (2018) The potential of P2X7 receptors as a therapeutic target, including inflammation and tumour progression. *Purinergic Signal.* **14**, 1–18
17. Deussing, J. M., and Arzt, E. (2018) P2X7 receptor: a potential therapeutic target for depression? *Trends Mol. Med.* **24**, 736–747
18. Jorgensen, N. R. (2018) The purinergic P2X7 ion channel receptor-a 'repair' receptor in bone. *Curr. Opin. Immunol.* **52**, 32–38
19. Roger, S., Jelassi, B., Couillin, I., Pelegrin, P., Besson, P., and Jiang, L. H. (2015) Understanding the roles of the P2X7 receptor in solid tumour progression and therapeutic perspectives. *Biochim. Biophys. Acta* **1848**, 2584–2602
20. Kopp, R., Krautloher, A., Ramirez-Fernandez, A., and Nicke, A. (2019) P2X7 interactions and signaling - making head or tail of it. *Front Mol. Neurosci.* **12**, 183
21. Crivici, A., and Ikura, M. (1995) Molecular and structural basis of target recognition by calmodulin. *Annu. Rev. Biophys. Biomol. Struct.* **24**, 85–116
22. Roger, S., Pelegrin, P., and Surprenant, A. (2008) Facilitation of P2X7 receptor currents and membrane blebbing via constitutive and dynamic calmodulin binding. *J. Neurosci.* **28**, 6393–6401
23. Roger, S., Gillet, L., Baroja-Mazo, A., Surprenant, A., and Pelegrin, P. (2010) C-terminal calmodulin-binding motif differentially controls human and rat P2X7 receptor current facilitation. *J. Biol. Chem.* **285**, 17514–17524
24. Cheewatrakoolpong, B., Gilchrest, H., Anthes, J. C., and Greenfeder, S. (2005) Identification and characterization of splice variants of the human P2X7 ATP channel. *Biochem. Biophys. Res. Commun.* **332**, 17–27
25. Tidow, H., and Nissen, P. (2013) Structural diversity of calmodulin binding to its target sites. *FEBS J.* **280**, 5551–5565
26. Alexander, C. G., Wanner, R., Johnson, C. M., Breitsprecher, D., Winter, G., Duhr, S., *et al.* (2014) Novel microscale approaches for easy, rapid determination of protein stability in academic and commercial settings. *Biochim. Biophys. Acta* **1844**, 2241–2250
27. Gao, K., Oerlemans, R., and Groves, M. R. (2020) Theory and applications of differential scanning fluorimetry in early-stage drug discovery. *Biophys. Rev.* **12**, 85–104
28. Burastero, O., Niebling, S., Defelipe, L. A., Gunther, C., Struve, A., and Garcia Alai, M. M. (2021) eSPC: an online data-analysis platform for molecular biophysics. *Acta Crystallogr. D Struct. Biol.* **77**, 1241–1250
29. Niebling, S., Burastero, O., Burgi, J., Gunther, C., Defelipe, L. A., Sander, S., *et al.* (2021) FoldAffinity: binding affinities from nDSF experiments. *Sci. Rep.* **11**, 9572
30. Panjkovich, A., and Svergun, D. I. (2018) CHROMIXS: automatic and interactive analysis of chromatography-coupled small-angle X-ray scattering data. *Bioinformatics* **34**, 1944–1946
31. Manalastas-Cantos, K., Konarev, P. V., Hajizadeh, N. R., Kikhney, A. G., Petoukhov, M. V., Molodenskiy, D. S., *et al.* (2021) Atsas 3.0: expanded functionality and new tools for small-angle scattering data analysis. *J. Appl. Crystallogr.* **54**, 343–355

32. Svergun, D. I. (1992) Determination of the regularization parameter in indirect-transform methods using perceptual criteria. *J. Appl. Crystallogr.* **25**, 495–503
33. Svergun, D. I., Barberato, C., and Koch, M. H. J. (1995) Crysol - a program to evaluate X-ray solution scattering of biological macromolecules from atomic coordinates. *J. Appl. Crystallogr.* **28**, 768–773
34. Franke, D., and Svergun, D. I. (2009) DAMMIF, a program for rapid ab-initio shape determination in small-angle scattering. *J. Appl. Crystallogr.* **42**, 342–346
35. Trewhella, J., Duff, A. P., Durand, D., Gabel, F., Guss, J. M., Hendrickson, W. A., *et al.* (2017) 2017 publication guidelines for structural modelling of small-angle scattering data from biomolecules in solution: an update. *Acta Crystallogr. D Struct. Biol.* **73**(Pt 9), 710–728